Available online at www.sciencedirect.com

SCIENCE DIRECT®

International Journal of Heat and Fluid Flow 24 (2003) 529–537

International Journal of
HEAT AND
FLUID FLOW

www.elsevier.com/locate/ijhff

Effect of co- and counter-swirl on the isothermal flow- and mixture-field of an airblast atomizer nozzle

K. Merkle *, H. Haessler, H. Büchner, N. Zarzalis

Chair of Combustion Technology, Engler-Bunte-Institut, University of Karlsruhe, Kaiserstrasse 12, 76128 Karlsruhe, Germany

Received 25 November 2002; accepted 12 March 2003

Abstract

Results of the performed experiments describe the influence of co- and counter-rotating airflows through the inner and outer ducts of an airblast atomizer on the turbulent flow and mixture field. Therefore, two different nozzles have been manufactured, which differ only in the orientation of rotation of the inner and outer airflow, and have been confined by a combustion chamber, which provides optical access for laser diagnostics. The isothermal flow field has been investigated using a 3D-LDV-system. The 30° off-axis forward scattering configuration allows a high temporal and spatial resolution of the three velocity components, thus determining not only mean velocities but the total Reynolds stress tensor. Determination of the mixture field has been performed by a suction probe and subsequent analysis of the local concentration by means of conventional gas analysis. Compared to the co-swirl configuration the flow field of the counter-swirl arrangement exhibits a marked increase of the mass flow recirculated in the internal recirculation zone and a reduction of its length in axial direction. The analysis of turbulence quantities shows a considerable attenuation of the turbulent exchange of momentum perpendicular to the main flow direction for counter-rotating airflows. According to Rayleigh's criterion this effect is attributed to the weaker reduction of the radial profiles of the time mean tangential velocity within the domain of the near-nozzle outer jet boundary in case of the counter-swirl configuration. In analogy to the exchange of momentum the obtained mixture fields feature a reduction of turbulent mass transfer rate in radial direction with counter-rotating airflows.

Keywords: Airblast atomizer; Turbulence; Co-swirl; Counter-swirl; Rayleigh criterion; Turbulent mixing; Swirl flows

---

1. Introduction

Many practical combustion devices employ swirling flows because formation of an internal recirculation zone enables high volumetric heat release rates in conjunction with excellent flame stability. To allow well-directed manipulation of particular flame properties, as flame stability or formation of pollutant emissions, extensive studies have been performed through the last decades, mainly covering single-swirl burners, see e.g. the overviews of Syred and Beér (1974) or Gupta et al. (1984).

Introduction of the swirling air through two or more concentric annuli offers additional degrees of freedom to control the radial distribution of flow and swirl for achieving significantly different combustion characteristics, as flow and mixing patterns, levels of turbulence, and different flame stability limits.

An example for the successful application of a multi-annular swirl burner with respect to pollutant emissions is given by Toqan et al. (1992), who utilized a strong radial density gradient in the swirling flow to perform a well-controlled combustion staging by an effective spatial separation of the fuel rich flame cone from the lean outer regions of a natural gas diffusion flame. Thereby the authors realized moderate temperature levels and extraordinarily low NO_x emissions.

Terasaki and Hayashi (1996) conducted an experimental comparison of a double- and a conventional single-swirler burner of non-premixed, direct fuel injection type. The reasons for the observed lower NO_x emissions are discussed on the basis of the measured fuel–air mixing under isothermal and the profiles of equivalence ratio and gaseous species concentrations

---

* Corresponding author. Tel.: +49-721-608-6025; fax: +49-721-661-501.

E-mail address: klaus.merkle@vbt.uni-karlsruhe.de (K. Merkle).

doi:10.1016/S0142-727X(03)00047-X

under reacting conditions. According to the authors the observed NO_x reduction under overall lean conditions can be attributed to the more rapid mixing process of fuel and air in the double-swirler burner compared to the conventional one.

On the basis of CCD flame photographs and time-resolved temperature measurements within an unconfined premixed flame Gupta et al. (1998) emphasized the importance of the radial distribution of swirl on the temperature distribution and flame instability. Gupta et al. (2001) extended the study of two different generic co-swirling double-swirl burners towards direct comparison of a co- and counter-swirl burner. Temperature fluctuations and subsequent calculated thermal micro time scales indicate a stronger radial exchange in case of the co-swirling burner.

Additional investigations on the effect of co- and counter-swirl nozzles have been performed by Ateshkadi et al. (1998) using a liquid fuelled airblast atomizer in a confined environment. They reported a marked increase of flame stability in case of the counter-swirl arrangement. The relatively poor stability of the co-swirl nozzle is explained by insufficient fuel in the recirculation region, where the counter-swirling atomizer features a large population of droplets which are held responsible for the good flame stability. Measurements of Durbin and Ballal (1996) conducted at a generic double-swirl step swirl combustor fuelled with methane and propane, respectively, yielded a strong dependence of flame shape, structure and location from the combination of outer and inner swirl. The observed difference in lean blowout for the co- and counter-swirling configurations appeared to depend on how the flame stabilizes. Counter-swirl conditions produced an attached flame for moderate inner swirl intensity, which is accompanied by better flame stability.

The present work is part of an experimental investigation, which aims at the characterization of the influence of co- and counter-swirling airflows on the lean stability limits of an airblast atomizer. The experiments have been conducted due to the remaining uncertainty regarding the mechanisms to which the sense of rotation of the distinct airflows affect the formation of different flow and mixture fields. Considering their crucial importance with respect to lean blowout, measurements on the isothermal jets have been conducted as a first step. The results of this study are subject of the present paper.

2. Experimental setup

The experiments were carried out using an atmospheric airblast atomizer in a cylindrical combustion chamber with optical access for LDV measurements. A sketch of the system under investigation is given in Fig. 1. The atomizer consists of a modular arrangement of two radial swirl generators, an atomizer lip which separates the two airstreams from each other within the nozzle, and an air diffuser with a throat diameter of $D_0 = 2R_0$.

To provide identical fluid mechanical boundary conditions for both the isothermal flow and mixture fields, methane was fed through an annular gap within the atomizer lip also throughout the LDV measurements determining the flow field of the investigated nozzles. The presented work is meant to be extended onto reacting flows in a subsequent stage of the investigation using natural gas as fuel. Therefore, methane does not

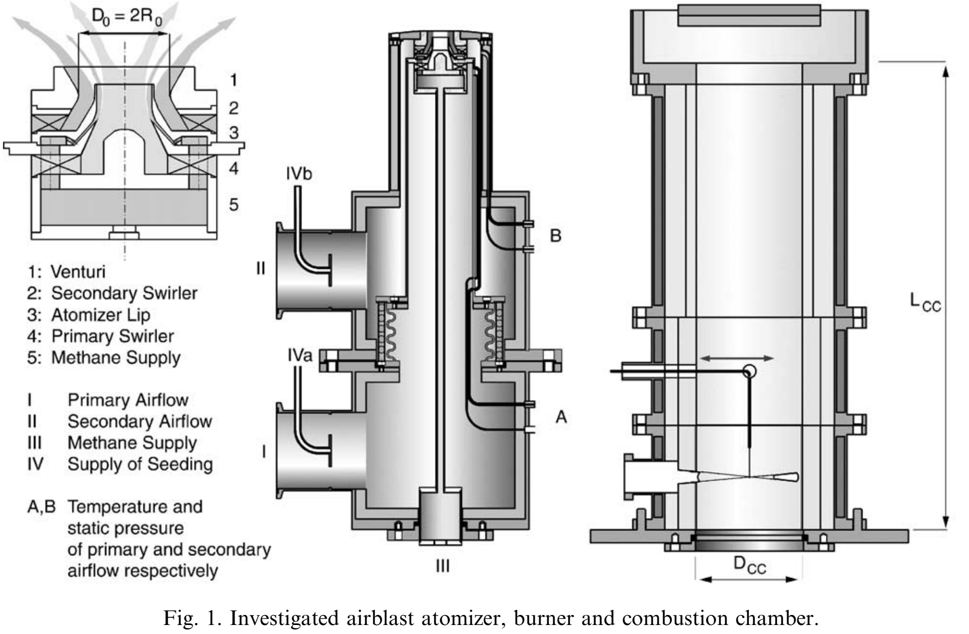

Fig. 1. Investigated airblast atomizer, burner and combustion chamber.

Table 1
Operating conditions for selected test cases

	T_A (°C)	$\dot{M}_A$ (kg/h)	Re	λ	$\Delta p_i = \Delta p_o$ (mbar)	$x_i = \dot{M}_{A,i}/\dot{M}_{A,o}$	S_i	S_o
Co-swirl	50	64	60 000	2	30	0.31	0.46	1
Counter-swirl	50	64	60 000	2	30	0.31	0.46	−1

just serve as a tracer for mixture field measurements, but is fed in considerable quantities corresponding to an air equivalence ratio of $\lambda = 2$. This approach allows the expected variations between isothermal and reacting flow and mixture fields to be attributed solely to the combustion and subsequent thermal expansion of the flow, since inflow conditions are kept nearly constant for the isothermal and reacting jet.

Consequently, the conception of the nozzle fitting allows the mass flow rate and the preheat temperature of primary and secondary airflow to be adjusted independently from each other. Methane is delivered to the atomizer through a central pipe along the axis of the nozzle holder. The primary airflow is fed at the lower half of the nozzle holder and gets surrounded by secondary air, which is supplied through a connecting section at the upper half of the nozzle assembly. Furthermore, the supply with seeding particles and control points of temperature and static pressure for each airflow are depicted. Optical access to the cylindrical burning chamber is enabled by flat quartz-glass-windows, which are positioned with respect to the chosen LDV arrangement. Moreover, four connecting sections are attached to the combustion chamber to provide access for suction probe measurements. The diameter of the combustion chamber is $D_{CC} = 4D_0$, its length is limited by an annular ring outlet at $L_{CC} = 4.5D_{CC}$. This outlet geometry avoids back-flow through the exit section, which otherwise could be induced by the lowered pressure on the axis of the rotating fluid. Access to different radial measurement positions is permitted by horizontal adjustment of the LDV system relative to the combustion chamber. Axial adjustment was realized by vertical displacement of the nozzle assembly within the chamber. At axial positions $x/D_0 > 1$ the two lower segments of the chamber were exchanged in their order.

For both airflows a constant air preheat temperature of $T_A = 50$ °C has been selected. The mass flow rates of air and methane were adjusted to $\dot{M}_A = 64$ kg/h and $\dot{M}_M = 1.8$ kg/h, corresponding to a thermal load of 29 kW, and an air equivalence ratio $\lambda_0 = 2$. The Reynolds number is calculated as the product of the axial average air velocity at the nozzle exit and the throat diameter of the diffuser divided by the kinematic viscosity of the air at $T_A = 50$ °C ($Re = U_0 D_0/\nu_A$) and yields approximately 60 000. The proportion of the airflow through primary and secondary swirler $\dot{M}_{A,i}$ and $\dot{M}_{A,o}$ has been adjusted so as to reach equal values of pressure loss $\Delta p = 30$ mbar for both inner and outer channel and yields $x_i = \dot{M}_{A,i}/\dot{M}_A = 0.31$ for the inner duct. Theoretical swirl numbers $S_{0,th}$ of the inner as well as the outer airflow S_i and S_o are calculated according to Leuckel (1967), using only geometry data of the swirl generators, as the ratio of angular to axial momentum flux divided by the radius of the outer burner throat R_0 for both inner and outer channel. Operating conditions are summarized in Table 1.

The isothermal flow field was determined by adding magnesium oxide particles of 0.7–1.2 μm in diameter to both airflows. Time-resolved measurements of the three velocity components have been conducted using a commercial 3-D DANTEC-LDV in a 30° off-axis forward scattering configuration with a focal length of 500 mm. This configuration yields high signal to noise ratios of the forward scattered light and allows reduction of the measurement volume to an ellipsoid of approximately 150 μm in diameter and 350 μm in length. A multi-line argon ion laser (INNOVA 70) at a typical operating output power of 0.5 W was employed as light source. At each location roughly 20 000 samples of the instantaneous velocity vector were used to subsequently calculate the three mean velocity components and all six Reynolds stress components. Measurements of the mixture fields have been conducted employing a suction probe of 1 mm outer diameter (see Fig. 1) and subsequent analysis of the local concentration by means of conventional gas analysis.

3. Results and discussion

3.1. Mean velocities

To give an impression of the time mean flow pattern, isolines of the stream function are shown for both co- and counter-swirl in Fig. 2. The streamlines are plotted in increments of 20% with respect to the inlet flow rate. Regions of negative and small values of the stream function are shaded dark. To relate the location of the flow features to the nozzle geometry, a sketch of the atomizer mouth is drawn alongside the ordinate of the plot. Due to the confinement of the flow an outer recirculation zone exists, where roughly 184% of the net mass flux fed through the nozzle are revolved. The inner recirculation zone stretches symmetrically to the axis and shows a large toroidal vortex. In axial direction the internal recirculation zone extends upstream right into the outlet section of the atomizer, its downstream

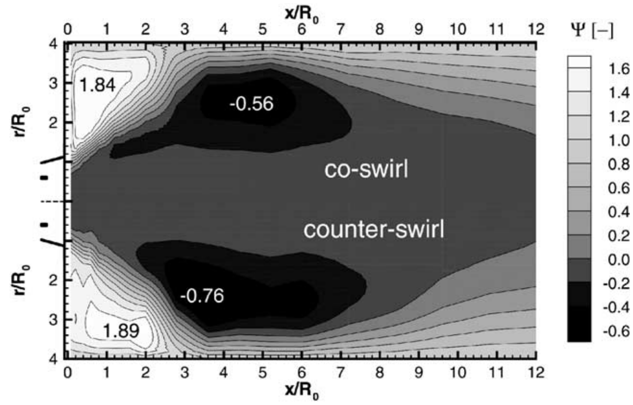

Fig. 2. Stream function of both co- and counter-swirl configuration (flow direction from left to right).

stagnation point is located outside the measuring range at $x/R_0 > 12$. Maximum recirculation amounts to 56% of the input mass flux and is located at $x/R_0 \approx 4.5$ downstream the nozzle at a radial position of $r/R_0 \approx 2.5$. Caused by the displacement effect of the wide-stretched structure of the vortex breakdown bubble, the downstream propagating fluid is deviated towards the wall of the chamber, so that in an axial distance of $x/R_0 \approx 4$ from the inlet 80% of the total mass flux passes the chamber on radii $r/R_0 > 0.36$. Further downstream the airflow shifts towards a more uniform distribution across the cross section of the chamber.

The impact of counter-rotating swirl is shown in the lower half of Fig. 2. The shape and size of the outer recirculation zone remain nearly unaffected by the sense of rotation. Caused by the smaller values of the radial velocity component the jet emanating from the nozzle impinges slightly further downstream upon the wall, thus enhancing the outer recirculated mass flow from 184% to 189%. The internal recirculation zone is strongly influenced by the orientation of swirl. The maximum value of the recirculated mass flux exceeds 75% of the net inflow, but in return it seems to be reduced in length, as indicated at axial distances $x/R_0 > 10$.

In Fig. 3 a clipping of the near nozzle part of the flow field is magnified and displayed as a vector plot. Every vector represents the sum of the local axial and radial velocity components in all measured positions. This graph clearly shows an additional vortex in the case of counter-swirl arrangement, located in the wake of the atomizer lip at $x/R_0 \approx 0.3$ and $r/R_0 \approx 0.5$. The described characteristics of the flow field can also be identified in the profiles of the mean velocity components revealed in Fig. 4, each normalized with the average nozzle exit velocity U_0. Here and in the following U, V, W denote the mean velocities in axial, radial and tangential directions in cylindrical coordinates and u, v, w their respective fluctuating portions.

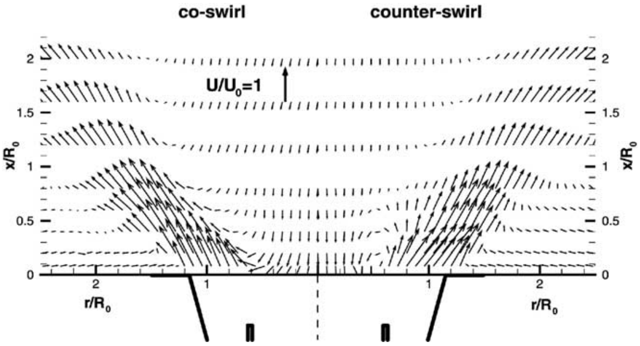

Fig. 3. UV-vectorplot of co- and counter-swirl configuration.

An explanation of these results is given in Fig. 5, where measured tangential velocities within the combustion chamber and qualitative distributions of tangential velocity and static pressure inside the atomizer for the co- and counter-swirl configuration are depicted. Firstly, the profiles are considered at an axial position within the nozzle x_0, where inner and outer airflow just start to merge together in the wake of the atomizer lip. Assuming in a first order approach, that interaction of the airflows is negligible in this plane, the tangential velocity profiles emanating from the inner duct of the atomizer are identical, since the geometry of the primary swirler is kept constant in both cases. The radial profiles of tangential velocity generated by the outer swirler are expected to be of the same shape, but of opposite sign. The tangential movement of fluid in axisymmetric flows induces centrifugal forces, which are balanced by a radial gradient of static pressure:

$$\frac{W^2}{r} = \frac{1}{\rho}\frac{\partial p}{\partial r} \tag{1}$$

Thus, it generates a minimum of pressure at the symmetric axis and a positive pressure gradient towards the jet boundary. Considering the above mentioned simplifications, the static pressure within the nozzle at the location $x = x_0$, $r = 0$ is independent of the sense of rotation of the flows. Due to the divergence of the jet and conservation of angular momentum flux a decline of W and resulting centrifugal forces are observed further downstream. Therefore, the static pressure p rises with growing distance, i.e. a positive pressure gradient along the axis is generated. When exceeding a characteristic value, the latter causes a reversal of the flow direction near the axis so that negative axial velocities U are observed along the line of symmetry. At the counter-swirl arrangement an additional decay of tangential velocity maxima is superimposed on the effect of jet divergence, as the inversely orientated fluxes of angular momentum from the inner and outer duct of the nozzle partially compensate each other. Taking into account that the initial values of $p(r = 0)$ in the plane $x = x_0$ have similar values, the counter-swirl configuration produces a

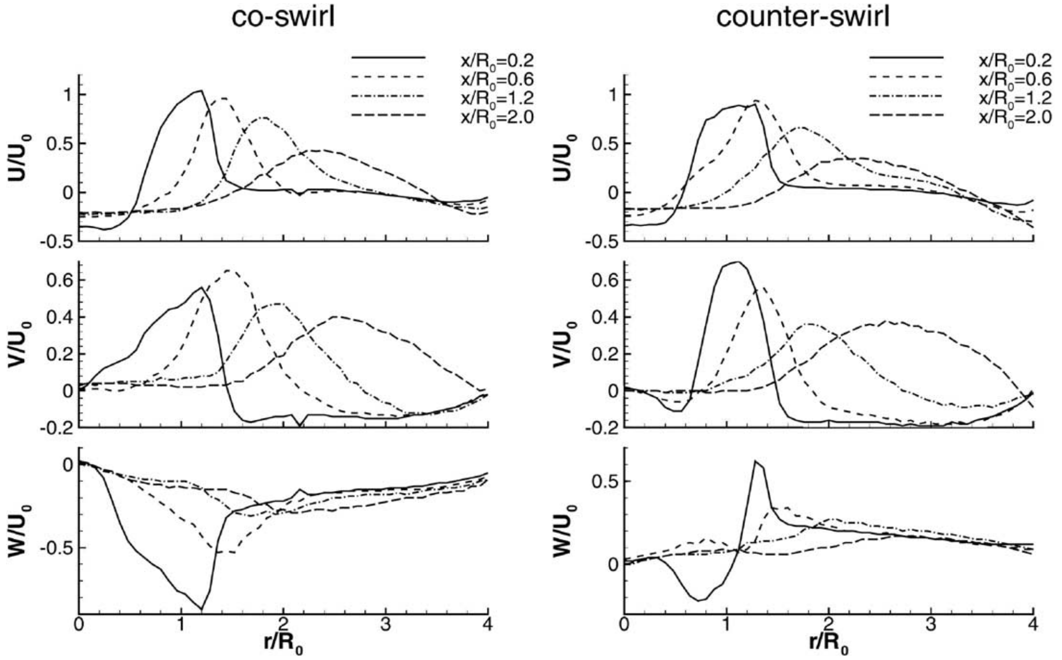

Fig. 4. Normalized mean velocities at co- and counter-swirl.

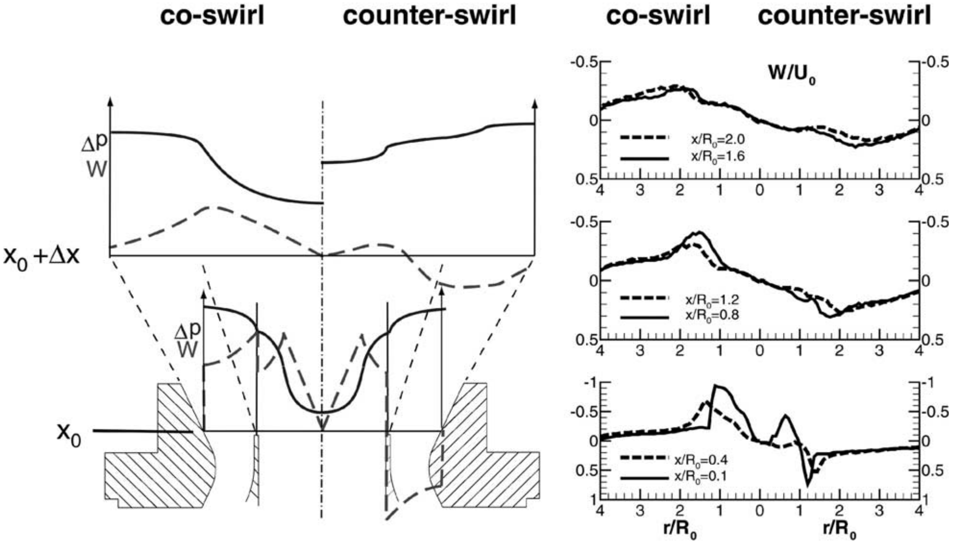

Fig. 5. Tangential velocity W and presumed profiles of static pressure.

stronger axial pressure gradient, and therefore an enhancement of the internal recirculation is observed.

3.2. Turbulence quantities

Fig. 6 reveals the profiles of the Reynolds normal stress components u_{RMS}, v_{RMS} and w_{RMS}, each normalized with the mean nozzle exit velocity U_0. The turbulent kinetic energy k, which is defined as the halved sum of the normal stress components, is also calculated as a summing-up. In both test cases, the identity $v_{\mathrm{RMS}}(r/R_0 = 0) = w_{\mathrm{RMS}}(r/R_0 = 0)$, deduced from the axisymmetry condition of the flow, is well satisfied. As a common feature, u_{RMS} and w_{RMS} display a discrete maximum, whose radial position is defined by the intense production of turbulence in the shear region at the outer boundary of the internal recirculation zone, where the respective gradients $\mathrm{d}U/\mathrm{d}x$, $\mathrm{d}V/\mathrm{d}r$ and V/r reach high values. Further downstream no such steep velocity gradients have been found, thus the normal stress components decay and are convected with the annular jet towards higher radii. As a peculiarity the near nozzle

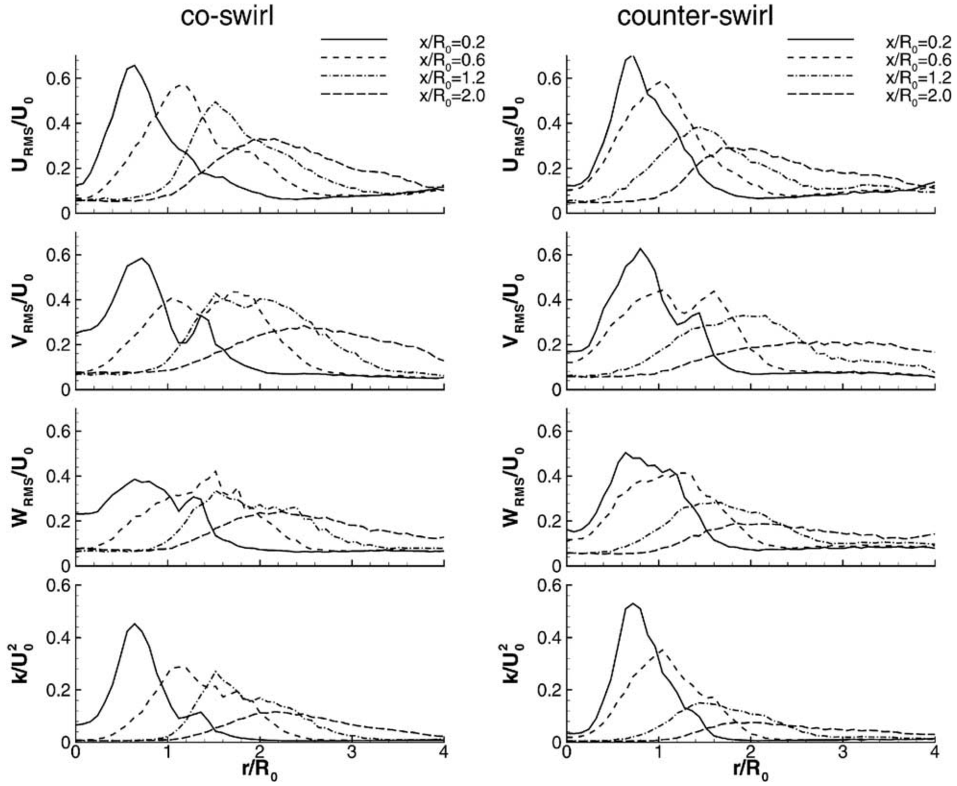

Fig. 6. Measured normalized Reynolds normal stresses and turbulent kinetic energy at co- and counter-swirl conditions.

profiles of v_{RMS} are marked by a second maximum corresponding to the steep gradient $\mathrm{d}V/\mathrm{d}r$ at the outer boundary of the downstream propagating jet. Comparison of the co- and counter-swirling configuration shows that the counter-swirl reaches higher values of turbulent kinetic energy k only in the immediate vicinity of the atomizer. This is mainly due to good accordance of the radial positions of the maxima of all three normal stress components. Further downstream a faster decrease than in the co-swirl case is observed, so that at axial distances of $x/R_0 > 1$ significant lower values of k have been measured throughout the cross section of the chamber. It seems noteworthy that starting from $x/R_0 = 0.4$ the maximum of k is restricted to a smaller radial section of the chamber, i.e. even in the region, where the co-swirl arrangement yields lower values of k, these cover a larger radial domain and tend to form a second maximum on higher radii, less pronounced than the inner one. In case of the counter-swirl arrangement the latter can be identified by a terrace-like region of the turbulence energy profile.

Considerations, which offer an explanation to this behaviour, are based on Rayleigh's stability criterion (Rayleigh, 1917). A mass element, propagating on a circular path, can either tend to amplify or to dampen an initial perturbation, depending on the velocity of the neighbouring fluid elements. The vortex on the left hand side in Fig. 7 is characterized by a linear increase of W by the radius. A turbulence element m_1, deflected from the radius r_1 to r_2, keeps its initial specific angular momentum $\Gamma_1 = W_1 r_1$, which results in a minor tangential velocity $W_{1^*} = \Gamma_1/r_2$ compared to the ambient fluid ($W_2 = \Gamma_2/r_2$). Thus, the centrifugal force acting on this element, $F_{1^*} = \rho W_{1^*}^2/r_2 \sim \Gamma_1^2/r_2^3$ is smaller than the force resulting from the local pressure gradient at the radius r_2 (see Eq. (1)): $F_2 = \rho W_2^2/r_2 \sim \Gamma_2^2/r_2^3$. This causes a tendency to lead the mass element m_1 back on smaller radii. This damping effect on turbulence is always expected, when the profile of specific angular momentum is marked by an increase of Γ^2 with increasing radius. This occurs at any velocity profile $W \sim r^n$ with an exponent $n > -1$, i.e. any profile that exhibits an increase of W with r (e.g. solid body vortex, $n = 1$) or a decrease which is lesser than that of the free vortex ($n = -1$). For a steeper decrease the opposite effect, an enhancement of turbulent exchange is observed, as illustrated on the right hand side of Fig. 7. Leuckel (1970) reported an increase of exchange coefficients of mass and momentum of one order in magnitude in flows with negative gradients $\mathrm{d}\Gamma^2/\mathrm{d}r$ compared to flows with $\mathrm{d}\Gamma^2/\mathrm{d}r > 0$ in good agreement with experiments of Holzäpfel et al. (1996), whereas e.g. Holzäpfel et al. (1999) observed a damping effect of the solid body vortex on turbulent exchange.

In Fig. 8 profiles of $\mathrm{d}\Gamma^2/\mathrm{d}r$, calculated from the mean tangential velocity W near the nozzle mouth, are plotted against the radius for both co- (left) and counter-swirl-

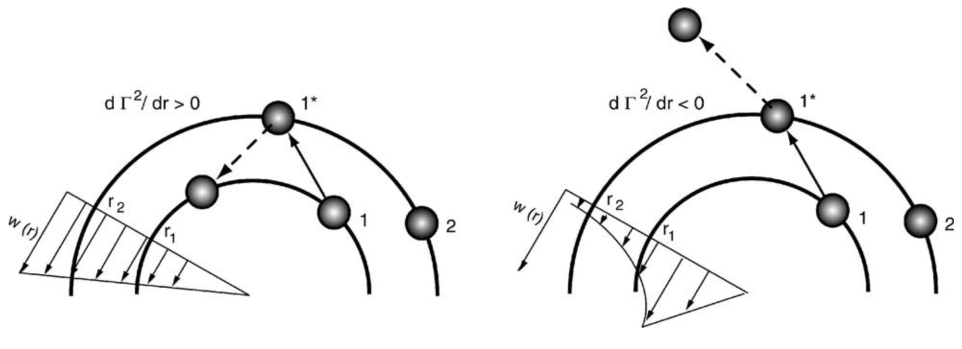

Fig. 7. Tangential velocity profile and dampening (left) and enhancing (right) influence on turbulence.

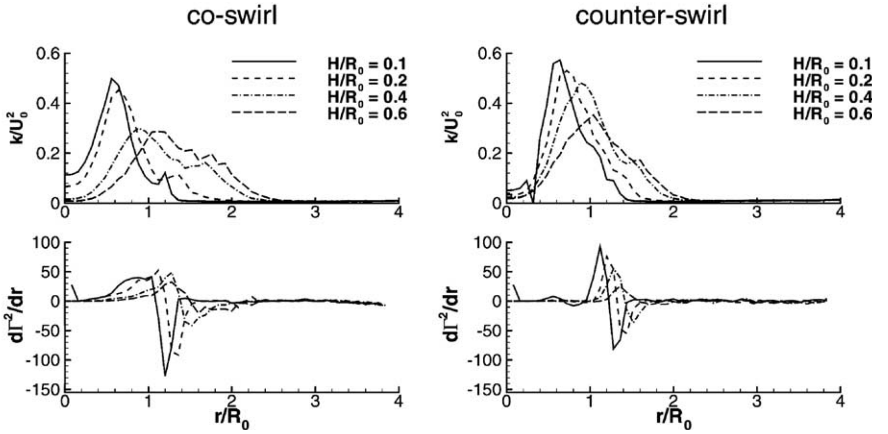

Fig. 8. Normalized turbulent kinetic energy and radial gradient of squared angular momentum.

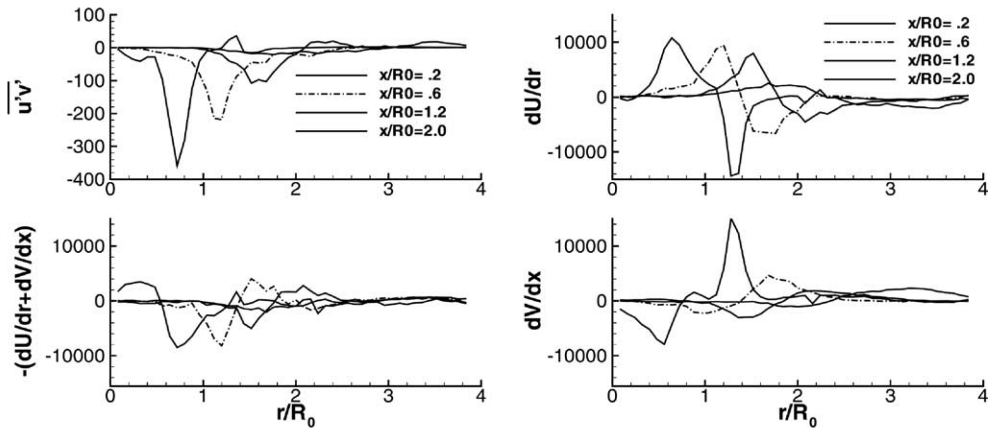

Fig. 9. Measured shear stress at $\overline{u'v'}$ and corresponding gradients of mean velocities at co-swirl configuration.

ing flows (right). The inner maximum of $d\Gamma^2/dr$ is caused by the solid body vortex region, which accompanies the inner boundary of the downstream propagating jet. As can be seen from the good agreement of the local minima of v_{RMS} and the turbulent kinetic energy k, it acts as a damper concerning turbulent exchange. The following minimum of $d\Gamma^2/dr$ corresponds to the steep decrease of W at the outer jet boundary. The radial positions of the outer k-maxima and the minima of $d\Gamma^2/dr$ also yield good agreement, thus confirming the validity of the Rayleigh criterion.

A discussion of the measured shear stresses concludes the current section. Measured turbulent shear stresses $\overline{u'v'}$ in the jet-dominated region of the co-swirl flow field are depicted in the upper left of Fig. 9, whereas the graph underneath illustrates the gradients of the corresponding mean velocities according to the gradient hypothesis $-(dU/dr + dV/dx)$. The right hand side of

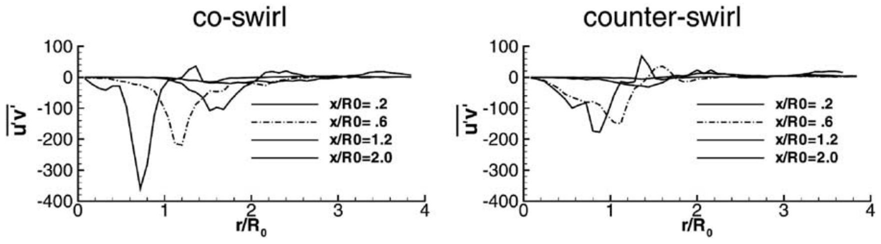

Fig. 10. Measured shear stress $\overline{u'v'}$ for both configurations.

Fig. 9 displays the latter split into its single components. As these plots show, $\mathrm{d}U/\mathrm{d}r$ and $\mathrm{d}V/\mathrm{d}x$ are of the same order of magnitude in the jet-dominated domain, and act in opposite direction on the resulting shear stress. Considering that convective and diffusive transport of turbulence which affect the distribution of turbulent kinematic viscosity $\nu_{\mathrm{t,rx}}$ throughout the flow field cannot be accounted for in the experimental data, a reasonable agreement of the gradient hypothesis and measured correlation $\overline{u'v'}$ is obtained.

The boundary condition of rotationally symmetric flows $\overline{u'v'}(r=0)=0$ is well satisfied for both test cases (see Fig. 10). Any deviation from this behaviour would yield turbulent transport across the axis which would be inconsistent with the expected and observed symmetry of the flow field. With further radial progression $\overline{u'v'}$ forms a minimum, whose position is defined by the steep gradient of $\mathrm{d}U/\mathrm{d}r$ at the boundary of the inner recirculation zone, then passes a relative maximum of either positive or negative sign, caused by the above mentioned interaction of radial decrease of U and axial increase of V along the outer boundary of the jet, and slowly approaches zero. Quantitative comparison of $\overline{u'v'}$ for co- and counter-swirl arrangement again yields stronger turbulent exchange of axial momentum flux in radial direction in the case of the co-swirl atomizer.

3.3. Turbulent mixing

In Fig. 11 enlarged clippings of the mixture fields generated by co- and counter-swirl atomizer are presented. Herein, isolines of the local air equivalence ratio λ are plotted in increments of 0.15. The global air equivalence ratio, derived from the inflowing mass fluxes of air and methane, is kept constant at $\lambda_0 = 2$ in both cases. Thus, regions of almost complete macro-mixing are marked by local air ratios $\lambda(x,r)$ around 2, whereas larger deviations from that value indicate regions of incomplete fuel–air mixing. Within these graphs, the outer air flows of both atomizers are easily identified by values of $\lambda > 2$, which are in accordance with the geometry of the nozzle. The inner airflow and the methane are already premixed to a great part when entering the combustion chamber, so that the regions, where λ falls beyond unity, are restricted to small areas in close vicinity to the atomizer. In both cases the process of macro-mixing is nearly completed one nozzle diameter downstream the flow field. Compared to the counter-swirl arrangement in case of co-swirl, a faster decay of excess air in the wake of the secondary channel, as well as of excess fuel carried by the primary airflow, is observed. Furthermore, deviation of λ within the outer recirculation zone amounts less than 5% of λ_0, whereas the counter-swirl arrangement is characterized by a noticeable shortage of methane in the same region. These findings confirm the expectation that, in analogy to turbulent exchange of momentum, turbulent mass exchange is also dampened by application of counter-swirling airflows.

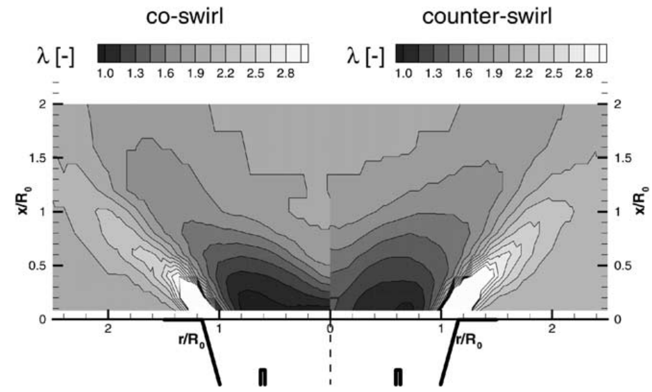

Fig. 11. Mixture field of both configurations.

4. Conclusions

Compared to the co-swirl configuration the flow field of the counter-swirl arrangement exhibits a marked increase of the mass flow recirculated in the internal recirculation zone and a reduction of its length in axial direction. This is attributed to the faster decay of tangential velocity maxima in case of counter-rotating airflows, induced by partial compensation of inversely orientated angular momentum fluxes. These generate a stronger positive axial pressure gradient $\mathrm{d}p/\mathrm{d}x$, thus enhancing the internal recirculation zone. The outer recirculation zone remains nearly unaffected by the direction of swirl.

Analysis of local turbulence quantities yields a restriction of turbulent exchange to smaller radial sections and lower maximum values in the jet-dominated domain of the flow field in case of counter-swirling airflows. These findings are due to a steeper radial increase of absolute values of tangential velocity in the domain of the solid body vortex, which accompanies the inner boundary of the downstream propagating jet. Within the region of the outer jet boundary, *W*-profiles of the counter-rotating arrangement are characterized by a lesser decrease of absolute values of *W* compared to co-swirl. In accordance to Rayleigh's criterion, which considers the forces of radial pressure gradient and centrifugal forces acting on a turbulence element deviated from its initial track, application of counter-swirl therefore constitutes a stronger dampening along the inner and a weaker enforcement of turbulence intensity along the outer jet boundary compared to the co-swirl flow field.

Comparison of the mixture fields exhibits faster macro-mixing of fuel and combustion air in case of the co-swirl arrangement. These findings confirm the observation that turbulent exchange is dampened by application of counter-swirling airflows.

References

Ateshkadi, A., McDonell, V.G., Samuelson, G.S., 1998. Effect of hardware geometry on gas and drop behavior in a radial mixer spray. In: 27th Symposium (International) on Combustion, pp. 1985–1992.

Durbin, M.D., Ballal, D.R., 1996. Studies of lean blowout in a step swirl combustor. Journal of Engineering for Gas Turbines and Power 118, 72–77.

Gupta, A.K., Lilley, D.G., Syred, N., 1984. Swirl Flows. Abacus Press.

Gupta, A.K., Lewis, M.J., Qi, S., 1998. Effect of swirl on combustion characteristics in premixed flames. Journal of Engineering for Gas Turbines and Power 120, 488–494.

Gupta, A.K., Lewis, M.J., Daurer, M., 2001. Swirl effects on combustion characteristics of premixed flames. Journal of Engineering for Gas Turbines and Power 123, 619–626.

Holzäpfel, F., Lenze, B., Leuckel, W., 1996. Swirl-induced intermittency: a novel effect modifying the turbulence structure of swirling free jets. In: 26th Symposium (International) on Combustion, pp. 187–194.

Holzäpfel, F., Lenze, B., Leuckel, W., 1999. Quintuple hot-wire measurements of the turbulence structure in confined swirling flows. Journal of Fluids Engineering 121, 517–525.

Leuckel, W., 1967. Swirl intensities, swirl types and energy loss of different swirl generating devices. IFRF-Doc. G02/a/16.

Leuckel, W., 1970. Further experiments on turbulent exchange in swirling flows through air annual channel. IFRF-Doc. G02/a/19.

Rayleigh, Lord, 1917. On the dynamics of revolving fluids. Proceedings of the Royal Society, Series A 93, 148–154.

Syred, N., Beér, J.M., 1974. Combustion in swirling flows: a review. Combustion and Flame 23, 143–201.

Terasaki, T., Hayashi, S., 1996. The effects of fuel–air mixing on NO_x formation in non-premixed swirl burners. In: 26th Symposium (International) on Combustion, pp. 2733–2739.

Toqan, M.A., Beèr, J.M., Jansohn, J., Sun, N., Testa, A., Shihadeh, A., Teare, J.D., 1992. Low NO_x-emissions from radially stratified natural gas–air turbulent diffusion flames. In: 24th Symposium (International) on Combustion, pp. 1391–1399.